Mechanical
Sciences

Elastodynamic modeling and analysis of a 4SRRR overconstrained parallel robot

Baoyu Wang[1], Yiyang Zhao[2], Chao Yang[3], Xudong Hu[1], and Yanzheng Zhao[2]

[1]School of Mechanical Engineering, Zhejiang Sci-Tech University, Hangzhou,
Zhejiang province, 310018, China
[2]School of Mechanical Engineering, Shanghai Jiao Tong University, Shanghai, 200240, China
[3]College of Mechanical and Electrical Engineering, Jiaxing University, Jiaxing,
Zhejiang province, 314001, China

Correspondence: Xudong Hu (xdhu@zstu.edu.cn) and Yanzheng Zhao (yzh-zhao@sjtu.edu.cn)

Abstract. To address the unstructured on-site work requirements in shipyards and large-steel-structure manufacturing plants, this paper develops a 4SRRR (where S is spherical and R is rotational) quadruped wall-climbing robot, establishes a dynamic analytical model, and analyzes its natural frequencies. First, Timoshenko beam elements, which consider shear deformation, are used to replace Euler–Bernoulli beam elements, and the dynamic control equations for each element are established. The Lagrangian equation is then used to derive the dynamic control equations for the rods. Second, based on the theory of multipoint constraint elements and linear algebra, a set of independent displacement coordinates is established for the connection points between rods and the moving platform, rods and rods, and rods and the fixed platform. The global independent generalized displacement coordinates of the mechanism are obtained by combining these independent displacement coordinates with the internal node displacement coordinates. Third, the overall dynamic control equations of the mechanism are obtained by combining the Lagrangian equation with the global independent generalized displacement coordinates. Comparing the results with the finite element method (FEM) established using Ansys software, it is found that even when the rods are considered single elements the error in the first three natural frequencies does not exceed 3.5 %. When the rods are divided into three elements, the error in the first six natural frequencies does not exceed 5 %. Further increasing the number of rod divisions results in diminishing reductions in the error.

1 Introduction

With the development of high-end manufacturing fields such as shipbuilding and port machinery, the demand for unstructured on-site tasks like welding and grinding has become increasingly urgent. A heavy-load quadruped wall-climbing robot can transport welding robots, grinding robots, and similar equipment to specified on-site locations and can serve as a base to support these robots during operations. Welding and grinding robots require high operational precision, which necessitates that the quadruped wall-climbing robot used as the base must possess high stiffness performance. Natural frequency is one of the critical indicators in robot design. The higher the natural frequency (particularly the first-order natural frequency), the more significantly the robot's vibration response can be reduced. Suppressing robot vibrations is a major technical challenge that needs to be addressed in robot design. Establishing an accurate dynamic model of the robot is a crucial foundation for achieving dynamic behavior regulation and vibration suppression in robots (Yang et al., 2021).

Natural frequency is an inherent property of a mechanism and is closely related to its structural parameters and configuration. The key to calculating natural frequencies is to establish the global stiffness and mass matrices of the mechanism, combined with the constraint equations for solving the system (Germain et al., 2015; Hoevenaars et al., 2020; Taghvaeipour et al., 2015). Over the past few decades, scholars both domestically and internationally have conducted in-depth research on the natural frequency analysis of parallel

mechanisms. The methods for establishing dynamic models can be broadly classified into three categories: finite element method (FEM), experimental methods (EMs), and analytical methods (AMs).

In the FEM, the rods and joints can retain their actual shape and size, resulting in relatively stable and accurate outcomes (Kermanian et al., 2019), which are favored by engineers and technicians. Cheng and Wang (2012) employed the FEM to analyze the static and dynamic models of a four-degrees-of-freedom parallel mechanism. Son et al. (2010) utilized the FEM to analyze the dynamic performance of a three-degrees-of-freedom reconfigurable parallel robot and validated the FEM results with experimental data. Ma et al. (2016) analyzed the natural frequency distribution of parallel mechanisms throughout the workspace using a combination of CAD (computer-aided design) and CAE (computer-aided engineering). This method allows the finite element model to be automatically updated as the mechanism's position changes through batch processing. However, as the mechanism's position changes, the finite element model requires remeshing and recalculation, which is costly and thus generally used to verify the accuracy of analytical models.

EMs involve obtaining the natural frequency response function, as well as displacement and stress output responses, through experimental analysis. Zhang et al. (2009) measured the frequencies and modes of a 3PRR (where P is prismatical and R is rotational) plane-parallel mechanism via EMs and designed an optimal drive vibration control. Nguyen et al. (2019) analyzed the dynamic performance of a six-degrees-of-freedom industrial robot through EMs. EMs take into account the effects of key factors such as gaps and friction, resulting in accurate outcomes. However, EMs require precise testing equipment, are complex to operate, and are costly. Therefore, EMs are generally used in the final testing stage of prototypes or to verify the accuracy of analytical models.

AMs establish the dynamic control equations of parallel mechanisms over the entire domain through analytical expressions, thereby obtaining the distribution of the dynamic performance of the mechanisms throughout the domain. The main AMs include the virtual joint method (VJM), matrix structural analysis (MSA), and the assumed modes method (AMM). The VJM describes the inertia and flexibility of components by treating them as pseudo-rigid bodies supported by six-degrees-of-freedom springs (Venkiteswaran and Su, 2016; Zhu and Yu, 2017; Luo et al., 2014). Vu and Kuo (2019) used the VJM to establish the dynamic equations of a planar serial mechanism under gravity and external loads. Mei and Zhao (2018) developed the dynamic model of a 6RSS parallel mechanism based on the VJM. Although the VJM is computationally simple, it often struggles to account for platform flexibility and the shear deformation of rods, leading to lower accuracy. The MSA method borrows key ideas from the FEM by dividing components into larger finite elements, achieving high computational ac-

curacy with less time (Cammarata et al., 2013; Lvov et al., 2018; Hou et al., 2020). Pham et al. (2017) developed the dynamic model of a flexible plane-parallel mechanism using MSA and analyzed the distribution of the first-order natural frequency in the workspace. Zhang and Zhao (2015) and Zhang et al. (2016) established the dynamic model of a 3PRS parallel mechanism using MSA and substructure synthesis techniques. Wu et al. (2018) and Zhao et al. (2011) used MSA to establish the dynamic equations of 8PSS and TriMule robots, obtaining the natural frequency distribution in the workspace. MSA strikes a good balance between computational time and accuracy. However, existing MSA approaches use Euler–Bernoulli beam elements, neglecting the effects of shear deformation, and lack research on the extraction method of global independent generalized coordinates. The AMM assumes the deformation of the rods as a linear superposition of their first few modes. Sheng et al. (2019), Korayem et al. (2019), Yu and Chen (2019), Lochan et al. (2018), and Liang et al. (2017) developed the dynamic equations of plane-parallel mechanisms based on the AMM. The AMM can analyze the forced vibration problems of damped and non-conservative systems, but it is challenging to assume accurate mode shapes for complex mechanisms. Furthermore, the aforementioned analyses have not extended the AMM to spatial parallel and hybrid mechanisms.

The contributions of this paper are threefold. First, the paper replaces Euler–Bernoulli beam elements with Timoshenko beam elements that consider shear deformation to analyze the expanded constrained screw of the rods, obtaining the true elastic deformation of the rods and establishing stiffness and mass matrices that reflect the actual elastic deformation of the rods. Second, based on the theory of multipoint constraint elements and linear algebra, a general method for extracting global independent generalized displacement coordinates is developed, and the Lagrangian equation is used to formulate the dynamic control equations for a 4SRRR parallel wall-climbing robot. The global independent generalized displacement coordinates established include all constraints between objects and between objects and the base, with clear physical meaning, allowing direct evaluation of the mechanism's dynamic performance without the need to solve constraint equations or add Lagrange multipliers. Finally, based on the proposed model, a method for rapidly evaluating the fundamental frequency of parallel mechanisms is presented. This is achieved by investigating the effect of dividing the rods into different numbers of elements on the natural frequencies of the parallel mechanisms. This method simplifies the modeling process for natural frequency analysis and improves the efficiency of fundamental frequency calculations.

The structure of this paper is arranged as follows. Section 2 provides the kinematic description and inverse analysis of the 4SRRR quadruped wall-climbing robot. Section 3 establishes the elastic dynamic equations of the mechanism.
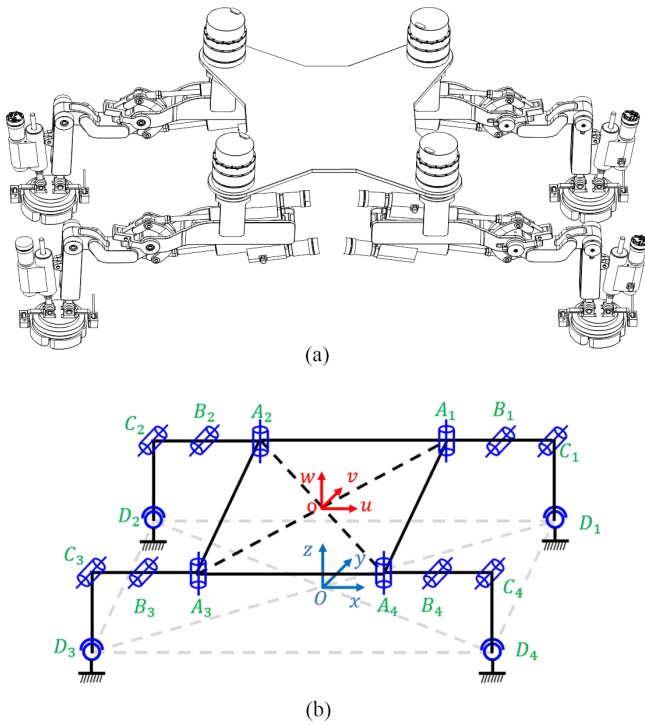
(a)

(b)

Figure 1. 4SRRR parallel robot: **(a)** 3D design diagram, **(b)** mechanism schematic diagram.

Section 4 presents the finite element verification and numerical analysis. Section 5 concludes the paper.

2 Mechanism description

As shown in Fig. 1a, the quadruped wall-climbing robot (4SRRR parallel robot) is developed to meet the needs of unstructured on-site work requirements for large and complex structural components. The schematic diagram is shown in Fig. 1b; the robot consists of a moving platform, a fixed platform (when the quadruped wall-climbing robot reaches the working position, the fixed feet and the working wall form the fixed platform), and four identical SRRR limbs. The limbs are symmetrically distributed, and each limb comprises three active rotational joints (R) and one passive spherical joint (S). The parallel robot has a total of 12 active rotational joints as the input to the mechanism. The physical and structural parameters of the robot are shown in Table 1.

The moving coordinate system $\{o-uvw\}$ has its origin at the geometric center of the moving platform of the robot, the w axis is perpendicular to the plane of the moving platform, the u axis is parallel to the line connecting points A_3 and A_4, and the v axis is determined by the right-hand rule. The fixed coordinate system $\{O-xyz\}$ has its origin at the geometric center of the fixed platform of the robot, the z axis points vertically upward, the x axis is parallel to the line connecting
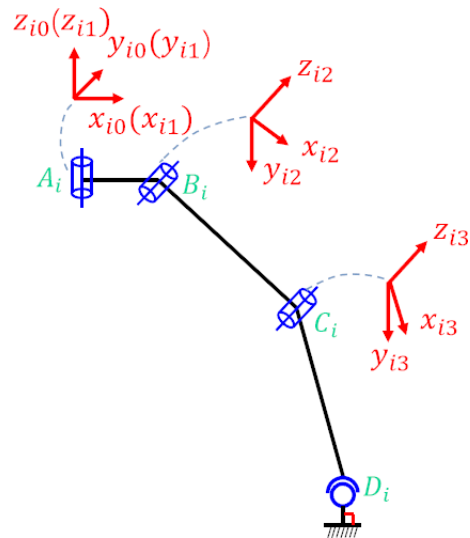

Figure 2. Limb coordinate system of the 4SRRR parallel robot.

points D_3 and D_4, and the y axis is determined by the right-hand rule.

As shown in Fig. 2, the limbs of the robot are connected to the moving platform at points A_i via R joints (with axes perpendicular to the surface of the moving platform) and to the fixed platform at points D_i via S joints. The local coordinate systems $\{A_i - x_{i1}y_{i1}z_{i1}\}$, $\{B_i - x_{i2}y_{i2}z_{i2}\}$, and $\{C_i - x_{i3}y_{i3}z_{i3}\}$ have their z_{i1}, z_{i2}, and z_{i3} axes aligned along the axes of A_i, B_i, and C_i, respectively. The x_{i1}, x_{i2}, and x_{i3} axes point in the directions of A_iB_i, B_iC_i, and C_iD_i, respectively.

The foot must be perpendicular to the work surface due to the magnetic suction when the 4SRRR parallel robot is attracted to the work surface. Figure 3 illustrates the inverse kinematics calculation diagram of the limb of the 4SRRR parallel robot.

The coordinate of A_i in the moving coordinate system is $({}^ou_{A_i}, {}^ov_{A_i}, {}^ow_{A_i})$, and the coordinates of D_i is $({}^ou_{D_i}, {}^ov_{D_i}, {}^ow_{D_i})$. The following equation, according to the geometric relationships, is

$$\begin{cases} \eta_{i1} = a\tan 2\left({}^ov_{D_i} - {}^ov_{A_i}, {}^ou_{D_i} - {}^ou_{A_i}\right), \\ L_{A_iD_i} = \text{abs}\left[\left({}^ou_{D_i} - {}^ou_{A_i}\right) \big/ \cos(\eta_{i1})\right], \\ H_i = \text{abs}\left({}^ow_{A_i} - {}^ow_{D_i}\right), \\ L_{B_iD_i} = \sqrt{\left(L_{A_iD_i} - L_1\right)^2 + H_i^2}. \end{cases} \quad (1)$$

According to the cosine theorem,

$$\begin{cases} \eta_{3i} = \pi - a\cos\left(\frac{L_2^2 + L_3^2 - L_{B_iD_i}^2}{2L_2L_3}\right), \\ \beta_i = a\cos\left(\frac{L_2^2 + L_{B_iD_i}^2 - L_3^2}{2L_2L_{B_iD_i}}\right). \end{cases} \quad (2)$$

Then,

$$\eta_{i2} + \beta_i = a\tan 2\left(H_i, L_i - L_1\right). \quad (3)$$

Table 1. Physical and structural parameters of the 4SRRR parallel robot.

| Parameters		Units	Values
E	Elastic modulus of aluminum alloy	Pa	7.1×10^{10}
μ	Poisson's ratio of aluminum alloy		0.33
L_A	The length of rod $A_2 A_3$ or $A_4 A_1$	m	0.54
W_A	The length of rod $A_1 A_2$ or $A_3 A_4$	m	0.54
L_{p1}	The length of rod $A_i B_i$ ($i = 1, 2, 3$, and 4)	m	0.140
L_{p2}	The length of rod $B_i C_i$ ($i = 1, 2, 3$, and 4)	m	0.350
L_{p3}	The length of rod $C_i D_i$ ($i = 1, 2, 3$, and 4)	m	0.350
d_{p1}/D_{p1}	The inner diameter of rod $A_i B_i$ ($i = 1, 2, 3$, and 4)	m	0.054/0.070
d_{p2}/D_{p2}	The inner diameter of rod $B_i C_i$ ($i = 1, 2, 3$, and 4)	m	0.054/0.070
d_{p3}/D_{p3}	The inner diameter of rod $C_i D_i$ ($i = 1, 2, 3$, and 4)	m	0.054/0.070
T_h	The thickness of the moving platform	m	0.01
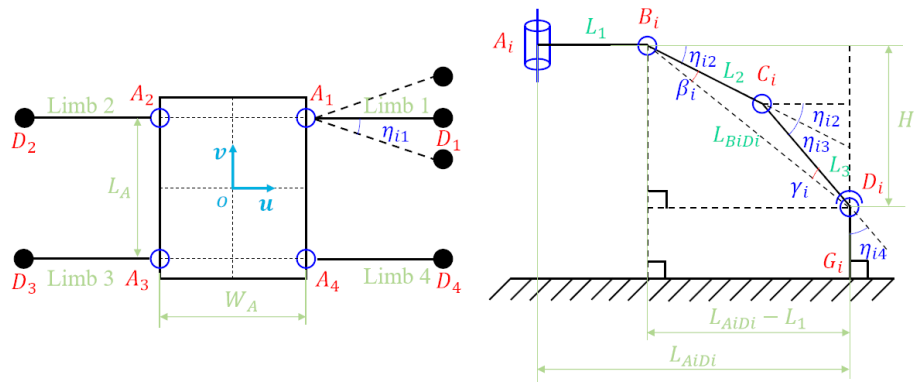
Figure 3. Inverse kinematics of the 4SRRR parallel robot.

We can then obtain

$$\begin{cases} \eta_{i2} = a \tan 2 (H_i, L_i - L_1) - \beta_i, \\ \eta_{i4} = \frac{\pi}{2} - \eta_{i2} - \eta_{i3}. \end{cases} \tag{4}$$

3   Elastodynamic model

The following assumptions are made for the parallel robot:

1. The fixed base, moving platform, motors, and all joints are rigid.

2. All joints are considered to be frictionless.

3. The rods are considered to be flexible, and the spatial composite deformation of the rods (including the tension (or compression), shear, torsional, and bending deformation components) is considered.

4. The deformation of all components is linear and within the elastic range.

3.1   Stiffness and mass matrices of one rod in the global coordinate

As shown in Fig. 4, the beam element has two nodal points at its ends, each possessing 6 degrees of freedom, result-
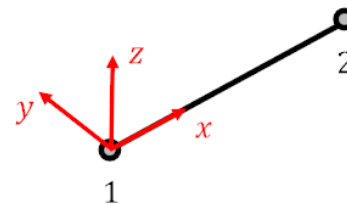

Figure 4. Timoshenko beam element.

ing in a total of 12 degrees of freedom. The column vector of the nodal points, which represents the generalized coordinates of the beam element, can be expressed as $X_e = [d_{e1}, r_{e1}, d_{e2}, r_{e2}]^\mathrm{T}$, where d_{e1} (r_{e1}) and d_{e2} (r_{e2}) denote the translational (rotational) displacements of nodes 1 and 2, respectively, in the element's coordinate system.

According to finite element theory, the stiffness matrix and the mass matrix of the beam element can be expressed as follows:

$$\begin{cases} \mathbf{K}_e = \int \int_{V_e} \int \mathbf{B}^\mathrm{T} \mathbf{D} \mathbf{B} \mathrm{d}V, \\ \mathbf{M}_e = \int \int_{V_e} \int \rho \mathbf{N}^\mathrm{T} \mathbf{N} \mathrm{d}V, \end{cases} \tag{5}$$

where $\mathbf{K}_e$ represents the element stiffness matrix; $\mathbf{M}_e$ represents the element mass matrix; V_e is the volume of the element; $\mathbf{B}$ is the strain-displacement transformation matrix and is given by $\boldsymbol{\varepsilon}_e = \mathbf{B}\boldsymbol{u}_e$, where $\boldsymbol{\varepsilon}_e = (\varepsilon_x \varepsilon_y \varepsilon_z \gamma_{xy} \gamma_{yz} \gamma_{zx})^{\mathrm{T}}$ is the strain column vector of the element; $\mathbf{D}$ denotes the elasticity matrix and is given by $\boldsymbol{\sigma}_e = \mathbf{D}\boldsymbol{\varepsilon}_e$, where $\boldsymbol{\sigma}_e = (\sigma_x \sigma_y \sigma_z \tau_{xy} \tau_{yz} \tau_{zx})^{\mathrm{T}}$ is the stress column vector of the element; ρ is the material density; and $\mathbf{N}$ is the shape function matrix and is given by $X_{\mathrm{ein}} = \mathbf{N}X_e$, where X_{ein} is the displacement column vector at any point within the element.

Constructing an element matrix that accurately reflects the true elastic deformation of the components is a key factor in establishing an accurate dynamic model of a parallel robot. To more precisely calculate the actual elastic deformation of the linkages, the beam element model employs a Timoshenko beam that accounts for shear deformation. The expressions for the element stiffness matrix and element mass matrix in the local coordinate system of the element can be derived as follows:

$$\mathbf{K}_e = \begin{pmatrix} \mathbf{K}_{e11} & \mathbf{K}_{e12} \\ \mathbf{K}_{e12}^{\mathrm{T}} & \mathbf{K}_{e22} \end{pmatrix}, \tag{6}$$

$$\mathbf{M}_e = \frac{\rho A L_e}{420} \begin{pmatrix} \mathbf{M}_{e11} & \mathbf{M}_{e12} \\ \mathbf{M}_{e12}^{\mathrm{T}} & \mathbf{M}_{e22} \end{pmatrix}, \tag{7}$$

where

$$\mathbf{K}_{e11} = \begin{pmatrix} \frac{EA}{L_e} & 0 & 0 & 0 & 0 & 0 \\ 0 & \frac{12EGI_z A_y}{L_e g_1} & 0 & 0 & 0 & \frac{6EGI_z A_y}{g_1} \\ 0 & 0 & \frac{12EGI_y A_z}{L_e g_2} & 0 & -\frac{6EGI_y A_z}{g_2} & 0 \\ 0 & 0 & 0 & \frac{GI_p}{L_e} & 0 & 0 \\ 0 & 0 & -\frac{6EGI_y A_z}{g_2} & 0 & \frac{4EI_y b_1}{L_e g_2} & 0 \\ 0 & \frac{6EGI_z A_y}{g_1} & 0 & 0 & 0 & \frac{4EI_z b_2}{L_e g_1} \end{pmatrix}, \tag{8}$$

$$\mathbf{K}_{e12} = \begin{pmatrix} -\frac{EA}{L_e} & 0 & 0 & 0 & 0 & 0 \\ 0 & -\frac{12EGI_z A_y}{L_e g_1} & 0 & 0 & 0 & \frac{6EGI_z A_y}{g_1} \\ 0 & 0 & -\frac{12EGI_y A_z}{L_e g_2} & 0 & -\frac{6EGI_y A_z}{g_2} & 0 \\ 0 & 0 & 0 & -\frac{GI_p}{L_e} & 0 & 0 \\ 0 & 0 & \frac{6EGI_y A_z}{g_2} & 0 & \frac{6EGI_y A_z L_e}{g_2} - \frac{4EI_y b_1}{L_e g_2} & 0 \\ 0 & -\frac{6EGI_z A_y}{g_1} & 0 & 0 & 0 & \frac{6EGI_z A_y L_e}{g_1} - \frac{4EI_z b_2}{L_e g_1} \end{pmatrix}, \tag{9}$$

$$\mathbf{K}_{e22} = \begin{pmatrix} \frac{EA}{L_e} & 0 & 0 & 0 & 0 & 0 \\ 0 & \frac{12EGI_z A_y}{L_e g_1} & 0 & 0 & 0 & -\frac{6EGI_z A_y}{g_1} \\ 0 & 0 & \frac{12EGI_y A_z}{L_e g_2} & 0 & \frac{6EGI_y A_z}{g_2} & 0 \\ 0 & 0 & 0 & \frac{GI_p}{L_e} & 0 & 0 \\ 0 & 0 & \frac{6EGI_y A_z}{g_2} & 0 & \frac{4EI_y b_1}{L_e g_2} & 0 \\ 0 & -\frac{6EGI_z A_y}{g_1} & 0 & 0 & 0 & \frac{4EI_z b_2}{L_e g_1} \end{pmatrix}, \tag{10}$$

$$\mathbf{M}_{e11} = \begin{pmatrix} 140 & 0 & 0 & 0 & 0 & 0 \\ 0 & 156 & 0 & 0 & 0 & 22L_e \\ 0 & 0 & 156 & 0 & -22L_e & 0 \\ 0 & 0 & 0 & 140I_p/A & 0 & 0 \\ 0 & 0 & -22L_e & 0 & 4L_e^2 & 0 \\ 0 & 22L_e & 0 & 0 & 0 & 4L_e^2 \end{pmatrix}, \tag{11}$$
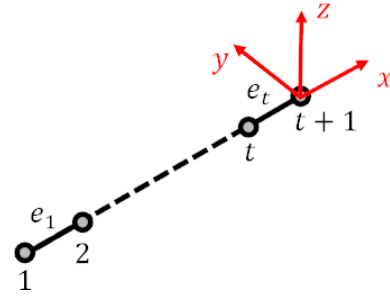

Figure 5. Finite element model of a rod.

$$\mathbf{M}_{e12} = \begin{pmatrix} 70 & 0 & 0 & 0 & 0 & 0 \\ 0 & 54 & 0 & 0 & 0 & -13L_e \\ 0 & 0 & 54 & 0 & 13L_e & 0 \\ 0 & 0 & 0 & 70I_p/A & 0 & 0 \\ 0 & 0 & -13L_e & 0 & -3L_e^2 & 0 \\ 0 & 13L_e & 0 & 0 & 0 & -3L_e^2 \end{pmatrix}, \tag{12}$$

$$\mathbf{M}_{e22} = \begin{pmatrix} 140 & 0 & 0 & 0 & 0 & 0 \\ 0 & 156 & 0 & 0 & 0 & -22L_e \\ 0 & 0 & 156 & 0 & 22L_e & 0 \\ 0 & 0 & 0 & 140I_p/A & 0 & 0 \\ 0 & 0 & 22L_e & 0 & 4L_e^2 & 0 \\ 0 & -22L_e & 0 & 0 & 0 & 4L_e^2 \end{pmatrix}, \tag{13}$$

where G is the shear modulus; I_x and I_y are the moments of inertia of the cross-section about the x and y axes, respectively; I_p and A represent the polar moment of inertia and the area of the cross-section, respectively; A_y and A_z are the effective shear areas of the cross-section along the y and z axis, respectively; L_e represents the length of the beam element; and $g_1 = GA_y L^2 + 12EI_z$, $g_2 = GA_z L^2 + 12EI_y$, $b_1 = GA_z L^2 + 3EI_y$, and $b_2 = GA_y L^2 + 3EI_z$.

The kinetic energy and elastic potential energy of the beam element can be expressed as follows:

$$\begin{cases} E_{\mathrm{ke}} = \frac{1}{2}\dot{X}_e^{\mathrm{T}}\mathbf{M}_e \dot{X}_e, \\ E_{\mathrm{pe}} = \frac{1}{2}X_e^{\mathrm{T}}\mathbf{K}_e X_e, \end{cases} \tag{14}$$

where E_{ke} and E_{pe} represent the kinetic energy and elastic potential energy of the beam element, respectively.

As shown in Fig. 5, considering the jth rod in limb i divided into t elements, where $e_k(k = 1, \ldots, t)$ represents the kth element, the generalized displacement coordinates of the jth rod of limb i can be expressed as follows:

$$^L X_{i,j} = \left(^L_{i,j,1}, ^L_{i,j,2}, \ldots, ^L_{i,j,t+1} \right)^{\mathrm{T}}_{6(t+1)\times 1}, \tag{15}$$

where $^L X_{r,i,j}$ represents the generalized displacement coordinates of the jth rod in limb i; the superscript "L" indicates that the vector is expressed in the local coordinate system; and $^L X_k(k = 1, \ldots, t+1)$ denotes the displacement coordinates of the kth node of the jth rod in limb i.

The mapping relationship between the displacement coordinates $^L X_{e,i,j,k}$ of the kth node of the jth rod in limb i and

the generalized displacement coordinates $^{L}X_{i,j}$ of the rod can be written as follows:

$$^{L}X_{e,i,j,k} = \mathbf{T}^{L}_{e,i,j,k}X_{i,j} \tag{16}$$

where $^{L}X_{e,i,j,k} = \left(^{L}X^{L}_{i,j,k}X_{i,j,k+1}\right)$ represents the displacement coordinates of the kth element of the jth rod in limb i in the local coordinate system, and $\mathbf{T}_{e,i,j,k}$ denotes the mapping matrix from the generalized displacement coordinates of the jth rod in limb i to the displacement coordinates of the kth element of the jth rod in limb i. Furthermore, we have

$$\begin{cases} \mathbf{T}_{e,i,j,1} = \begin{pmatrix} \mathbf{E}_6 & \mathbf{0}_6 & \cdots \\ \mathbf{0}_6 & \mathbf{E}_6 & \cdots \end{pmatrix}_{12\times(6t+6)}, \\ \mathbf{T}_{e,i,j,2} = \begin{pmatrix} \mathbf{0}_6 & \mathbf{E}_6 & \mathbf{0}_6 & \cdots \\ \mathbf{0}_6 & \mathbf{0}_6 & \mathbf{E}_6 & \cdots \end{pmatrix}_{12\times(6t+6)}, \\ \vdots \qquad \vdots \\ \mathbf{T}_{e,i,j,t} = \begin{pmatrix} \mathbf{0}_6 & \cdots & \mathbf{E}_6 & \mathbf{0}_6 \\ \mathbf{0}_6 & \cdots & \mathbf{0}_6 & \mathbf{E}_6 \end{pmatrix}_{12\times(6t+6)}, \end{cases} \tag{17}$$

where $\mathbf{E}_6$ is a 6×6 identity matrix, and $\mathbf{0}_6$ is a 6×6 zero matrix.

The kinetic energy and elastic potential energy of the e_k element, based on the generalized displacement coordinates of rod j of limb i, can be expressed as follows:

$$\begin{cases} E^{\text{ke}}_{e,i,j,k} \\ = \frac{1}{2}{}^{L}\dot{X}^{\text{T}}_{e,i,j,k}{}^{L}\mathbf{M}^{L}_{e,i,j,k}\dot{X}_{e,i,j,k} \\ = \frac{1}{2}{}^{L}\dot{X}^{\text{T}}_{i,j}\mathbf{T}^{\text{T}}_{e,i,j,k}{}^{L}\mathbf{M}_{e,i,j,k}\mathbf{T}^{L}_{e,i,j,k}\dot{X}_{i,j} \\ = \frac{1}{2}{}^{L}\dot{X}^{\text{T}}_{i,j}{}^{L}\mathbf{M}^{\text{r}}_{e,i,j,k}{}^{L}\dot{X}_{i,j}, \\ \qquad\qquad\qquad\qquad\qquad (k=1,\cdots,t) \\ E^{\text{pe}}_{e,i,j,k} \\ = \frac{1}{2}{}^{L}X^{\text{T}}_{e,i,j,k}{}^{L}\mathbf{K}^{L}_{e,i,j,k}X_{e,i,j,k} \\ = \frac{1}{2}{}^{L}X^{\text{T}}_{i,j}\mathbf{T}^{\text{T}}_{e,i,j,k}{}^{L}\mathbf{K}_{e,i,j,k}\mathbf{T}^{L}_{e,i,j,k}X_{i,j} \\ = \frac{1}{2}{}^{L}X^{\text{T}}_{i,j}{}^{L}\mathbf{K}^{\text{r}}_{e,i,j,k}{}^{L}X_{i,j}, \end{cases} \tag{18}$$

where $^{L}\mathbf{M}^{\text{r}}_{e,i,j,k} = \mathbf{T}^{\text{T}}_{e,i,j,k}{}^{L}\mathbf{M}_{e,i,j,k}\mathbf{T}_{e,i,j,k}$ and $^{L}\mathbf{K}^{\text{r}}_{e,i,j,k} = \mathbf{T}^{\text{T}}_{e,i,j,k}{}^{L}\mathbf{K}_{e,i,j,k}\mathbf{T}_{e,i,j,k}$ represent the mass contribution matrix and stiffness contribution matrix of the kth element of the jth rod in limb i, respectively.

Summing over Eq. (18) yields the kinetic energy and elastic potential energy of a single rod:

$$\begin{cases} E_{\text{ke},i,j} = \sum_{k=1}^{t} E^{\text{ke}}_{e,i,j,k} = \frac{1}{2}{}^{L}\dot{X}^{\text{T}}_{i,j}\left(\sum_{k=1}^{t}{}^{L}\mathbf{M}^{\text{r}}_{e,i,j,k}\right){}^{L}\dot{X}_{i,j} \\ \qquad = \frac{1}{2}{}^{L}\dot{X}^{\text{T}}_{i,j}{}^{L}\mathbf{M}^{L}_{i,j}\dot{X}_{i,j}, \\ E_{\text{pe},i,j} = \sum_{k=1}^{t} E^{\text{pe}}_{e,i,j,k} = \frac{1}{2}{}^{L}X^{\text{T}}_{i,j}\left(\sum_{k=1}^{t}{}^{L}\mathbf{K}^{\text{r}}_{e,i,j,k}\right){}^{L}X_{i,j} \\ \qquad = \frac{1}{2}{}^{L}X^{\text{T}}_{i,j}{}^{L}\mathbf{K}^{L}_{i,j}X_{i,j}, \end{cases} \tag{19}$$

where $^{L}\mathbf{M}_{i,j} = \sum_{k=1}^{t}{}^{L}\mathbf{M}^{\text{r}}_{e,i,j,k}$ and $^{L}\mathbf{K}_{i,j} = \sum_{k=1}^{t}{}^{L}\mathbf{K}^{\text{r}}_{e,i,j,k}$ represent the mass matrix and stiffness matrix of the rod in the local coordinate system, respectively.

The transformation matrix between the generalized displacement coordinates of the jth rod in limb i in the local coordinate system and the global coordinate system is defined as follows:

$$\dot{X}_{i,j} = \mathbf{D}^{L}_{i,j}\dot{X}_{i,j}, \tag{20}$$

where $\mathbf{D}_{i,j} = \text{diag}\left[\mathbf{R}_{i,j},\ldots,\mathbf{R}_{i,j}\right]^{\text{T}}$, and $\mathbf{R}_{i,j}$ represents the transformation matrix between the local coordinate system and the global coordinate system of the jth rod in limb i.

By substituting Eq. (20) into Eq. (19), the expressions for the kinetic and potential energy of rod j of limb i based on $X_{i,j}$ can be derived as follows:

$$\begin{cases} E_{\text{ke},i,j} = \frac{1}{2}\dot{X}^{\text{T}}_{i,j}\mathbf{D}^{\text{T}}_{i,j}{}^{L}\mathbf{M}_{i,j}\mathbf{D}_{i,j}\dot{X}_{i,j} = \frac{1}{2}\dot{X}^{\text{T}}_{i,j}\mathbf{M}_{i,j}\dot{X}_{i,j}, \\ E_{\text{pe},i,j} = \frac{1}{2}X^{\text{T}}_{i,j}\mathbf{D}^{\text{T}}_{i,j}{}^{L}\mathbf{K}_{i,j}\mathbf{D}_{i,j}X_{i,j} = \frac{1}{2}X^{\text{T}}_{i,j}\mathbf{K}_{i,j}X_{i,j}, \end{cases} \tag{21}$$

where $\mathbf{M}_{i,j} = \mathbf{D}^{L}_{i,j}\mathbf{M}_{i,j}\mathbf{D}^{\text{T}}_{i,j}$ and $\mathbf{K}_{i,j} = \mathbf{D}^{L}_{i,j}\mathbf{K}_{i,j}\mathbf{D}^{\text{T}}_{i,j}$ represent the mass matrix and stiffness matrix of the jth rod in limb i in the global coordinate system, respectively.

3.2 Mass matrix of the moving platform in the global coordinate system

Assuming the moving platform is rigid (Yu and Chen, 2019; Lochan et al., 2018), the kinetic energy of the moving platform can be obtained using the aforementioned method:

$$E_{\text{ko}} = \frac{1}{2}{}^{o}\dot{X}^{\text{T}o}_{o}\mathbf{M}^{o}_{o}\dot{X}_{o} = \frac{1}{2}\dot{X}^{\text{T}}_{o}\mathbf{D}^{o}_{o}\mathbf{M}_{o}\mathbf{D}^{\text{T}}_{o}\dot{X}_{o} = \frac{1}{2}\dot{X}^{\text{T}}_{o}\mathbf{M}_{o}\dot{X}_{o}, \tag{22}$$

$X_o = (d_o, r_o)^{\text{T}}$ and $^{o}X_o$ represent the displacement arrays of the exit node o of the moving platform in the global coordinate system and the local coordinate system $\{o\}$, respectively; $\mathbf{M}_o$ and $^{o}\mathbf{M}_o$ represent the mass matrix of the moving platform in the global coordinate system and the local coordinate system, respectively; and $\mathbf{D}_o = \text{diag}[\mathbf{R}, \mathbf{R}]$ is the transformation matrix for the displacement vector of the exit node of the

moving platform between the local coordinate system and the global coordinate system.

By using Eq. (22), we can obtain

$$\mathbf{M}_o = \mathbf{D}_o^o \mathbf{M}_o \mathbf{D}_o^{\mathrm{T}}. \tag{23}$$

3.3 Mass and stiffness matrices of the parallel robot in the global coordinate system

The global independent extended generalized displacement coordinates of the 4SRRR parallel robot can be expressed as

$$X = \left[X_{C_1 D_1}^{\mathrm{T}}, X_{B_1 C_1}^{\mathrm{T}}, X_{A_1 B_1}^{\mathrm{T}}, X_{C_2 D_2}^{\mathrm{T}}, X_{B_2 C_2}^{\mathrm{T}}, X_{A_2 B_2}^{\mathrm{T}}, \right.$$
$$\left. X_{C_3 D_3}^{\mathrm{T}}, X_{B_3 C_3}^{\mathrm{T}}, X_{A_3 B_3}^{\mathrm{T}}, X_{C_4 D_4}^{\mathrm{T}}, X_{B_4 C_4}^{\mathrm{T}}, X_{A_4 B_4}^{\mathrm{T}}, X_o \right]^{\mathrm{T}}, \tag{24}$$

where $X_{A_i B_i}$, $X_{B_i C_i}$, and $X_{C_i D_i}$ represent the global independent generalized displacement coordinates of rods $A_i B_i$, $B_i C_i$, and $C_i D_i$ in limb i, respectively.

The limbs of the 4SRRR parallel robot are connected to the moving platform, between limbs, and to the fixed platform through different joints. The exit nodes of the elements at the connections must satisfy certain constraint conditions. Therefore, the extended generalized displacement coordinates alone are insufficient to describe the physical properties of the mechanism; the constraint equations must be combined to extract the global independent generalized displacement coordinates of the mechanism. Correct extraction of the global independent generalized coordinates under different joint constraints is key to establishing an accurate dynamic model of the parallel robot.

Given the assumption that the moving platform is a rigid body, we have $r_{A_i} = r_o$. Additionally, considering that all three active joints (R joints) of the 4SRRR parallel robot are locked, the boundary conditions at A_i for limb i can be expressed as

$$X_{A_i} = \begin{bmatrix} d_{A_i} \\ r_{A_i} \end{bmatrix} = \begin{bmatrix} \mathbf{E}_3 & [A_i o \times] \\ \mathbf{0}_3 & \mathbf{E}_3 \end{bmatrix} X_o, \tag{25}$$

where $\mathbf{E}_3$ is a 3×3 identity matrix, and $[A_i o \times]$ denotes the skew-symmetric matrix.

Similarly, rods $A_i B_i$ and $B_i C_i$, as well as rods $B_i C_i$ and $C_i D_i$, are connected at B_i and C_i through R joints. If all three active joints (R joints) of the 4SRRR parallel robot are locked, the boundary conditions at B_i and C_i for limb i can be expressed as

$$\begin{cases} X_{A_i B_i, B_i} = X_{B_i C_i, B_i} = X_{B_i}, \\ X_{B_i C_i, C_i} = X_{C_i D_i, C_i} = X_{C_i}. \end{cases} \tag{26}$$

Rod $C_i D_i$ is connected to the fixed platform at D_i through an S joint. Based on the deformation characteristics of the S joint, the boundary conditions are given as follows:

$$^{D_i} d_{D_i} = 0_{3 \times 1}. \tag{27}$$

Since the S joint coordinate system $\{D_i - x_i y_i z_i\}$ is parallel to the global coordinate system $\{O - xyz\}$, the boundary conditions at D_i for the limb are expressed the same way in both the global coordinate system and the local coordinate system. Thus, we have

$$d_{D_i} = 0_{3 \times 1}. \tag{28}$$

Based on the above analysis, the global independent generalized displacement coordinates of the 4SRRR parallel robot are defined as

$$X = \left(r_{D_1}^{\mathrm{T}}, X_{C_1 D_1, \mathrm{in}}^{\mathrm{T}}, X_{C_1}^{\mathrm{T}}, X_{B_1 C_1, \mathrm{in}}^{\mathrm{T}}, X_{B_1}^{\mathrm{T}}, X_{A_1 B_1, \mathrm{in}}^{\mathrm{T}}, \right.$$
$$r_{D_2}^{\mathrm{T}}, X_{C_2 D_2, \mathrm{in}}^{\mathrm{T}}, X_{C_2}^{\mathrm{T}}, X_{B_2 C_2, \mathrm{in}}^{\mathrm{T}}, X_{B_2}^{\mathrm{T}}, X_{A_2 B_2, \mathrm{in}}^{\mathrm{T}}, r_{D_3}^{\mathrm{T}},$$
$$X_{C_3 D_3, \mathrm{in}}^{\mathrm{T}}, X_{C_3}^{\mathrm{T}}, X_{B_3 C_3, \mathrm{in}}^{\mathrm{T}}, X_{B_3}^{\mathrm{T}}, X_{A_3 B_3, \mathrm{in}}^{\mathrm{T}}, r_{D_4}^{\mathrm{T}},$$
$$\left. X_{C_4 D_4, \mathrm{in}}^{\mathrm{T}}, X_{C_4}^{\mathrm{T}}, X_{B_4 C_4, \mathrm{in}}^{\mathrm{T}}, X_{B_4}^{\mathrm{T}}, X_{A_4 B_4, \mathrm{in}}^{\mathrm{T}}, X_o^{\mathrm{T}} \right)^{\mathrm{T}}. \tag{29}$$

By combining Eqs. (24) and (29), the mapping relationship between the displacement coordinates of the rods and the moving platform with the global generalized displacement coordinates can be obtained:

$$\begin{cases} X_{i,1} = X_{C_i D_i} = \left(X_{D_i}^{\mathrm{T}}, X_{C_i D_i, \mathrm{in}}^{\mathrm{T}}, X_{C_i}^{\mathrm{T}} \right)^{\mathrm{T}} = \mathbf{\Gamma}_{i,1} X \\ (i = 1, 2, 3, 4), \\ X_{i,2} = X_{B_i C_i} = \left(X_{C_i}^{\mathrm{T}}, X_{B_i C_i, \mathrm{in}}^{\mathrm{T}}, X_{B_i}^{\mathrm{T}} \right)^{\mathrm{T}} = \mathbf{\Gamma}_{i,2} X \\ (i = 1, 2, 3, 4), \\ X_{i,3} = X_{A_i B_i} = \left(X_{B_i}^{\mathrm{T}}, X_{A_i B_i, \mathrm{in}}^{\mathrm{T}}, X_{A_i}^{\mathrm{T}} \right)^{\mathrm{T}} = \mathbf{\Gamma}_{i,3} X \\ (i = 1, 2, 3, 4), \\ X_o = \mathbf{\Gamma}_o X. \end{cases} \tag{30}$$

$\mathbf{\Gamma}_{1,1} = \mathbf{\Gamma}_{C_1 D_1}$

$$= \begin{bmatrix} 0_{3 \times (72t-6)} \\ \mathbf{E}_3 & 0_{3 \times (72t-9)} \\ 0_{(6t-6) \times 3} & \mathbf{E}_{(6t-6)} & 0_{(6t-6) \times (66t-3)} \\ 0_{6 \times (6t-3)} & \mathbf{E}_6 & 0_{6 \times (66t-9)} \end{bmatrix}_{(6t+6) \times (72t-6)}, \tag{31}$$

$\mathbf{\Gamma}_{1,2} = \mathbf{\Gamma}_{B_1 C_1}$

$$= \begin{bmatrix} 0_{6 \times (6t-3)} & \mathbf{E}_6 & 0_{6 \times (66t-9)} \\ 0_{(6t-6) \times (6t+3)} & \mathbf{E}_{(6t-6)} & 0_{(6t-6) \times (60t-3)} \\ 0_{6 \times (12t-3)} & \mathbf{E}_6 & 0_{6 \times (60t-9)} \end{bmatrix}_{(6t+6) \times (72t-6)}, \tag{32}$$

$\mathbf{\Gamma}_{1,3} = \mathbf{\Gamma}_{A_1 B_1}$

$$= \begin{bmatrix} 0_{6 \times (12t-3)} & \mathbf{E}_6 & 0_{6 \times (60t-9)} \\ 0_{(6t-6) \times (12t+3)} & \mathbf{E}_{(6t-6)} & 0_{(6t-6) \times (54t-3)} \\ 0_{3 \times (72t-12)} & \mathbf{E}_3 & [A_1 o \times] \\ 0_{3 \times (72t-9)} & \mathbf{E}_3 \end{bmatrix}_{(6t+6) \times (72t-6)}, \tag{33}$$

$\mathbf{\Gamma}_{2,1} = \mathbf{\Gamma}_{C_2 D_2}$

$$= \begin{bmatrix} 0_{3 \times (72t-6)} \\ 0_{3 \times (18t-3)} & \mathbf{E}_3 & 0_{3 \times (54t-6)} \\ 0_{(6t-6) \times 18t} & \mathbf{E}_{(6t-6)} & 0_{(6t-6) \times 48t} \\ 0_{6 \times (24t-6)} & \mathbf{E}_6 & 0_{6 \times (48t-6)} \end{bmatrix}_{(6t+6) \times (72t-6)}, \tag{34}$$

$\Gamma_{2,2} = \Gamma_{B_2 C_2}$

$$= \begin{bmatrix} 0_{6\times(24t-6)} & \mathbf{E}_6 & 0_{6\times(48t-6)} \\ 0_{(6t-6)\times 24t} & \mathbf{E}_{(6t-6)} & 0_{(6t-6)\times 42t} \\ 0_{6\times(30t-6)} & \mathbf{E}_6 & 0_{6\times(42t-6)} \end{bmatrix}_{(6t+6)\times(72t-6)}, \quad (35)$$

$\Gamma_{2,3} = \Gamma_{A_2 B_2}$

$$= \begin{bmatrix} 0_{6\times(30t-6)} & \mathbf{E}_6 & 0_{6\times(42t-6)} \\ 0_{(6t-6)\times 30t} & \mathbf{E}_{(6t-6)} & 0_{(6t-6)\times 36t} \\ 0_{3\times(72t-12)} & \mathbf{E}_3 & [A_2 \boldsymbol{o} \times] \\ 0_{3\times(72t-9)} & \mathbf{E}_3 & \end{bmatrix}_{(6t+6)\times(72t-6)}, \quad (36)$$

$\Gamma_{3,1} = \Gamma_{C_3 D_3}$

$$= \begin{bmatrix} 0_{3\times(72t-6)} & & \\ 0_{3\times(36t-3)} & \mathbf{E}_3 & 0_{3\times(36t-3)} \\ 0_{(6t-6)\times(36t-3)} & \mathbf{E}_{(6t-6)} & 0_{(6t-6)\times(30t+3)} \\ 0_{6\times(42t-9)} & \mathbf{E}_6 & 0_{6\times(30t-3)} \end{bmatrix}_{(6t+6)\times(72t-6)}, \quad (37)$$

$\Gamma_{3,2} = \Gamma_{B_3 C_3}$

$$= \begin{bmatrix} 0_{6\times(42t-9)} & \mathbf{E}_6 & 0_{6\times(30t-3)} \\ 0_{(6t-6)\times(42t-3)} & \mathbf{E}_{(6t-6)} & 0_{(6t-6)\times(24t+3)} \\ 0_{6\times(48t-9)} & \mathbf{E}_6 & 0_{6\times(24t-3)} \end{bmatrix}_{(6t+6)\times(72t-6)}, \quad (38)$$

$\Gamma_{3,3} = \Gamma_{A_3 B_3}$

$$= \begin{bmatrix} 0_{6\times(48t-9)} & \mathbf{E}_6 & 0_{6\times(24t-3)} \\ 0_{(6t-6)\times(48t-3)} & \mathbf{E}_{(6t-6)} & 0_{(6t-6)\times(18t+3)} \\ 0_{3\times(72t-12)} & \mathbf{E}_3 & [A_3 \boldsymbol{o} \times] \\ 0_{3\times(72t-9)} & \mathbf{E}_3 & \end{bmatrix}_{(6t+6)\times(72t-6)}, \quad (39)$$

$\Gamma_{4,1} = \Gamma_{C_4 D_4}$

$$= \begin{bmatrix} 0_{3\times(72t-6)} & & \\ 0_{3\times(54t-9)} & \mathbf{E}_3 & 0_{3\times 18t} \\ 0_{(6t-6)\times(54t-6)} & \mathbf{E}_{(6t-6)} & 0_{(6t-6)\times(12t+6)} \\ 0_{6\times(60t-12)} & \mathbf{E}_6 & 0_{6\times 12t} \end{bmatrix}_{(6t+6)\times(72t-6)}, \quad (40)$$

$\Gamma_{4,2} = \Gamma_{B_4 C_4}$

$$= \begin{bmatrix} 0_{6\times(60t-12)} & \mathbf{E}_6 & 0_{6\times 12t} \\ 0_{(6t-6)\times(60t-6)} & \mathbf{E}_{(6t-6)} & 0_{(6t-6)\times(6t+6)} \\ 0_{6\times(66t-12)} & \mathbf{E}_6 & 0_{6\times 6t} \end{bmatrix}_{(6t+6)\times(72t-6)}, \quad (41)$$

$\Gamma_{4,3} = \Gamma_{A_4 B_4}$

$$= \begin{bmatrix} 0_{6\times(66t-12)} & \mathbf{E}_6 & 0_{6\times 6t} \\ 0_{(6t-6)\times(66t-6)} & \mathbf{E}_{(6t-6)} & 0_{(6t-6)\times 6} \\ 0_{3\times(72t-12)} & \mathbf{E}_3 & [A_4 \boldsymbol{o} \times] \\ 0_{3\times(72t-9)} & \mathbf{E}_3 & \end{bmatrix}_{(6t+6)\times(72t-6)}, \quad (42)$$

$$\Gamma_o = \begin{bmatrix} 0_{6\times(72t-12)} & \mathbf{E}_6 \end{bmatrix}_{6\times(72t-6)}, \quad (43)$$

where the dimensions of the matrix $\Gamma_{i,j}(i = 1, 2, 3, 4; j = 1, 2, 3)$ are $(6t + 6) \times (72t - 6)$, and $\mathbf{E}_i$ represents an identity matrix of size $i \times i$.

Based on Eqs. (21) and (30)–(43), the total kinetic and potential energy of the 4SRRR parallel robot can be derived:

$$\begin{cases} E_{ke} = \sum_{i=1}^{4} \sum_{j=1}^{3} E_{ke,i,j} + E_{ko} = \frac{1}{2} \dot{\boldsymbol{X}}^T \mathbf{M} \dot{\boldsymbol{X}}, \\ E_{pe} = \sum_{i=1}^{4} \sum_{j=1}^{3} E_{pe,i,j} = \frac{1}{2} \dot{\boldsymbol{X}}^T \mathbf{K} \dot{\boldsymbol{X}}, \end{cases} \quad (44)$$

where $\mathbf{M} = \sum_{i=1}^{4} \sum_{j=1}^{4} \mathbf{M}_{i,j}^g + \mathbf{M}_o^g$ and $\mathbf{K} = \sum_{i=1}^{4} \sum_{j=1}^{4} \mathbf{K}_{i,j}^g$ represent the overall mass and stiffness matrices of the 4SRRR parallel robot, respectively; $\mathbf{M}_{i,j}^g = \Gamma_{i,j}^T \mathbf{M}_{i,j} \Gamma_{i,j}$ and $\mathbf{M}_o^g = \Gamma_{i,j}^T \mathbf{M}_o \Gamma_{i,j}$ represent the contribution matrices of the jth rod in limb i and the moving platform to the overall mass matrix, respectively; and $\mathbf{K}_{i,j}^g = \Gamma_{i,j}^T \mathbf{K}_{i,j} \Gamma_{i,j}$ represents the contribution matrix of the jth rod in limb i to the overall stiffness matrix.

Equation (44) includes all the constraint and continuity conditions of the mechanism. Compared to the continuity conditions of the limbs and moving platform considered in reference Mei and Zhao (2018) and the additional Lagrange multipliers needed in reference Korayem et al. (2019), the dynamic equations established in this paper do not require supplementary constraint equations or Lagrange multipliers. This results in a more concise equation that better simulates the actual constraint conditions of the mechanism.

The circular frequencies and mode vectors of the system can be obtained by solving Eq. (45):

$$\begin{cases} \left(\mathbf{K} - \omega_i^2\right) \boldsymbol{\Phi}_i = 0, \\ \det\left(\mathbf{K} - \omega_i^2 \mathbf{M}\right) = 0, \end{cases} \quad (45)$$

where ω_i is the ith circular frequency of the system, measured in rad s^{-1}, which can be obtained by solving the second equation of Eq. (45), and $\boldsymbol{\Phi}_i$ is the corresponding mode vector, which can be obtained by solving the first equation of Eq. (45).

In engineering, the natural frequency is often represented by the number of vibrations per second, which is given by

$$f_i = \frac{\omega_i}{2\pi}, \quad (46)$$

where f_i is the ith natural frequency of the system, measured in hertz (Hz).

4   Finite element verification and numerical simulation

To verify the correctness and feasibility of the theoretical method presented in this paper, commercial finite element software Ansys was used for validation. In the Ansys model, the material and structural parameters were provided according to the parameters used in the theoretical model, as detailed in Table 1. The flexible limbs were modeled using

"Beam 188" elements based on Timoshenko theory, and the rigid joints were modeled using multipoint constraint (MPC) elements. Each MPC element consisted of two coincident nodes, each connecting to two interconnected elements. The moving platform and the base were set as rigid bodies. The mass matrix of the moving platform in the local coordinate system $\{o - uvw\}$ can be obtained through SolidWorks software.

$$^{o}M_{o} = \mathrm{diag}\,(8.1948.1948.1940.1990.1990.398)$$

$$(\mathrm{kg\,kg\,m}^{2}) \tag{47}$$

To verify the correctness of the theoretical model, finite element models were established by considering two typical poses of the 4SRRR parallel robot. Pose 1: $\theta_{i1} = 0°$, $\theta_{i2} = 10°$, and $\theta_{i3} = 70°$ ($i = 1, 2, 3, 4$). Pose 2: $\theta_{i1} = 45°$, $\theta_{i2} = 10°$, and $\theta_{i3} = 70°$ ($i = 1, 2, 3, 4$). For these two poses, the mode shapes (first six modes) obtained from the modal analysis using the FEM are shown in Fig. 5. The comparison of natural frequencies between the theoretical method (using different numbers of element divisions) and the FEM is shown in Table 2.

The results for pose 1 in Table 2 show that even when the rods are considered single elements, the relative errors between the natural frequencies obtained by the theoretical method and the FEM for the first, second, and third modes are only 1.020 %, 1.958 %, and 3.024 %, respectively. However, the errors for the fourth, fifth, and sixth modes are as high as 15.088 %, 16.517 %, and 18.915 %, respectively. When the rods are divided into three elements, the errors for the fourth, fifth, and sixth modes rapidly decrease to 3.849 %, 4.168 %, and 4.393 %. Further increasing the number of rod divisions results in no significant reduction in the error. Similar results are obtained for pose 2. The results obtained using the theoretical method are in good agreement with those obtained from the FEM, verifying the acceptability of the proposed theoretical model for natural frequency analysis. The finite element analysis results of the natural frequencies of the 4SRRR parallel robot are shown in Fig. 6.

For the two aforementioned postures, when the rods are divided into 10 elements, the comparison of natural frequencies between the theoretical model, subspace iteration method (SIM; Zhang and Lin, 2007), static condensation method (Guyan reduction; Zhang and Lin, 2007), and dynamic condensation method (Kuhar reduction; Zhang and Lin, 2007) is shown in Table 3. The SIM reached the set convergence error (1 %) after just one iteration, and compared to the calculation time of 0.02 s for the exact solution of the theoretical model the SIM reduced the calculation time to 0.005 s, lowering the computational cost by 75 %. The first-order natural frequency of the Guyan reduction matches the exact solution, but there is a significant deviation in the higher-order natural frequencies, making it suitable for scenarios focusing only on the first-order natural frequency. The Kuhar reduction matches the exact solution for the first three

natural frequencies but still exhibits considerable errors for higher-order natural frequencies.

In principle, continuous structures have an infinite number of natural frequencies. However, when calculating natural frequencies, we typically discretize the structure into a finite number of modes to solve the problem, with the lowest natural frequency being the fundamental frequency of the structure. It is well known that the fundamental frequency of a structure is very important information. Additionally, the fundamental frequency is related to the structure's vulnerability to resonance failure due to an external frequency load. In other words, if only the fundamental frequency of the mechanism is considered, the accuracy may meet engineering requirements when treating components as single elements. Consequently, the calculation process is significantly simplified, and the dimensions of the overall mass and stiffness matrices are reduced.

Figure 7 presents the MAC (modal assurance criterion) values of the first six modes for the theoretical and finite element solutions of the 4SRRR parallel robot in two typical poses. The diagonal elements in Fig. 7 are all equal to 1, indicating that the theoretical and finite element solutions are approximately identical for the two poses. This is consistent with the results in Table 2, further confirming the accuracy of the theoretical solution. According to Fig. 7a, the mode shape correlation coefficient between the fourth and sixth mode vectors for pose 1 of the quadruped wall-climbing robot is 1, indicating that these two mode vectors are very similar, while all other MAC matrix values are less than 0.12. According to Fig. 7b, the mode shape correlation coefficient between the fifth and sixth mode vectors for pose 2 is 0.62, and the correlation coefficient between the second and fifth mode vectors is 0.52, while all other MAC matrix values are less than 0.34.

In the global coordinate system, when the quadruped wall-climbing robot (4SRRR robot) is in pose 1 (pose 2), the geometric center point o of the moving platform moves within the arbitrarily selected working plane $z = 0.35\,\mathrm{m}$ ($z = 0.40546\,\mathrm{m}$) in the range of $x = -0.1 : 0.01 : 0.1$, $y = -0.1 : 0.01 : 0.1$. Figure 8 shows the distribution of natural frequencies of the 4SRRR robot moving within the plane for pose 1 and pose 2. As shown in Fig. 8, the natural frequencies of the 4SRRR robot in pose 1 and pose 2 are symmetrical about the x axis and y axis, respectively, which is consistent with the structure of the quadruped wall-climbing robot in these poses. Additionally, the natural frequencies of the 4SRRR robot vary in different poses. In engineering, the fundamental frequency, i.e., the first natural frequency, is often of greater concern. A higher fundamental frequency implies a higher control bandwidth, which can reduce the vibration response of the mechanism. Therefore, it is preferable to select the regions with a higher fundamental frequency as the working area. Compared to pose 1, the first natural frequency within the plane of motion in pose 2 is significantly higher, making pose 2 more suitable for on-site operations. More-
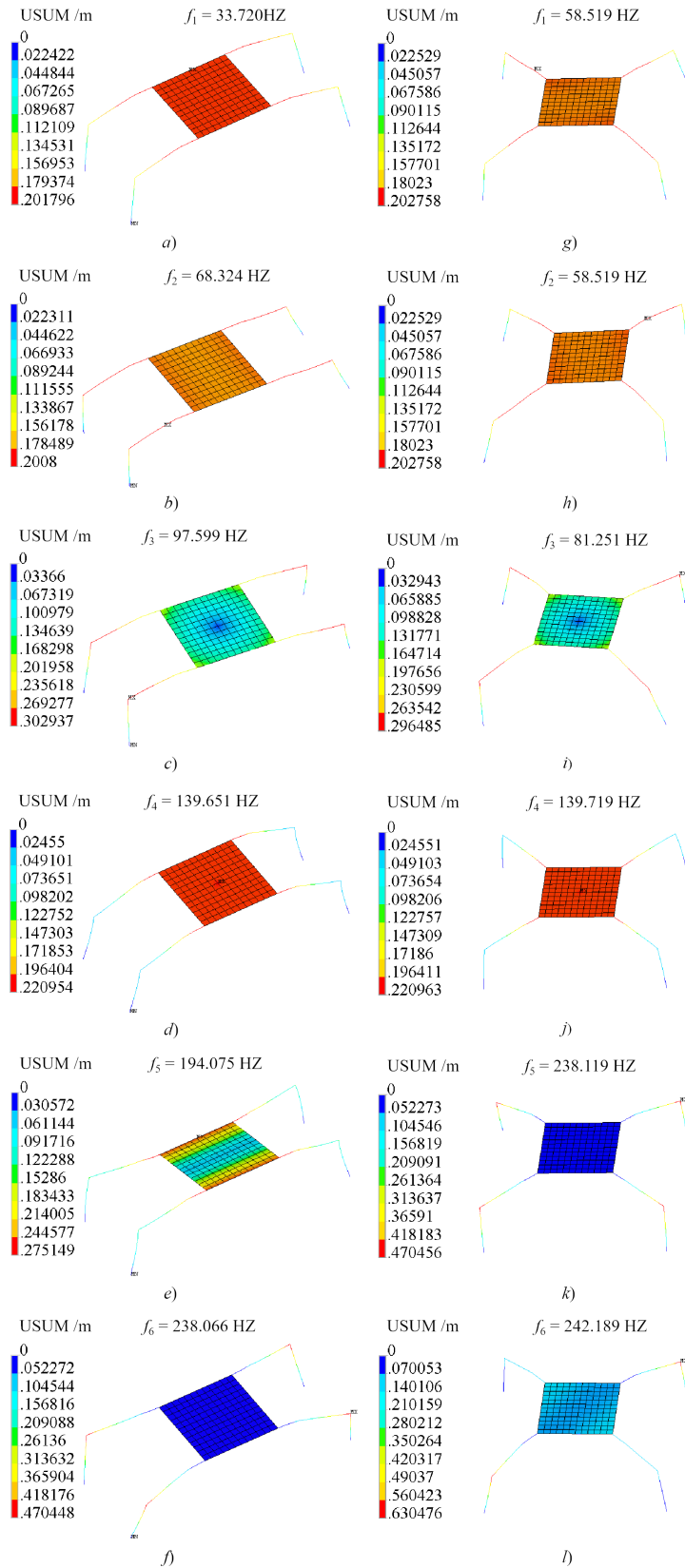
Figure 6. Modal analysis of the 4SRRR parallel robot with the FEM: **(a)** pose 1: f_1, **(b)** pose 1: f_2, **(c)** pose 1: f_3, **(d)** pose 1: f_4, **(e)** pose 1: f_5, **(f)** pose 1: f_6, **(g)** pose 2: f_1, **(h)** pose 2: f_2, **(i)** pose 2: f_3, **(j)** pose 2: f_4, **(k)** pose 2: f_5, and **(l)** pose 2: f_6.

Table 2. Comparison of natural frequency between the theoretical method and the FEM.

Pose	Method	f_1 (Hz)	f_2 (Hz)	f_3 (Hz)	f_4 (Hz)	f_5 (Hz)	f_6 (Hz)
1	FEM	33.720	68.324	97.599	139.651	194.075	238.066
	Theoretical ($t = 1$)	34.064	69.662	100.550	160.722	226.130	283.096
	Relative error (%)	1.020	1.958	3.024	15.088	16.517	18.915
	Theoretical ($t = 3$)	34.039	69.391	99.449	145.026	202.164	248.524
	Relative error (%)	0.946	1.561	1.896	3.849	4.168	4.393
	Theoretical ($t = 5$)	33.999	69.387	99.437	144.924	202.011	248.303
	Relative error (%)	0.827	1.556	1.883	3.776	4.089	4.300
	Theoretical ($t = 10$)	33.999	69.387	99.435	144.910	201.989	248.270
	Relative error (%)	0.827	1.556	1.881	3.766	4.078	4.286
2	FEM	58.519	58.519	81.251	139.719	238.119	242.189
	Theoretical ($t = 1$)	59.156	59.416	83.878	158.890	270.425	291.278
	Relative error (%)	1.088	1.532	3.233	13.721	13.567	20.269
	Theoretical ($t = 3$)	59.120	59.100	82.199	143.028	243.148	254.090
	Relative error (%)	1.027	0.992	1.167	2.368	2.112	4.914
	Theoretical ($t = 5$)	59.118	59.096	82.180	142.927	242.972	253.686
	Relative error (%)	1.024	0.986	1.143	2.296	2.038	4.747
	Theoretical ($t = 10$)	59.118	59.095	82.176	142.913	242.946	253.625
	Relative error (%)	1.024	0.984	1.139	2.286	2.027	4.722

Table 3. Comparison of natural frequency between the theoretical method and SIM, Guyan reduction, and Kuhar reduction.

| Pose	Method	f_1 (Hz)	f_2 (Hz)	f_3 (Hz)	f_4 (Hz)	f_5 (Hz)	f_6 (Hz)	Iterations	Time (s)
1	Theoretical	33.999	69.387	99.435	144.910	201.989	248.270	/	0.02
	SIM	34.002	69.397	99.520	145.094	202.385	248.486	1	0.005
	Guyan reduction	34.292	71.229	103.860	517.379	762.874	942.684	/	0.004
	Kuhar reduction	34.001	69.392	99.471	173.409	299.445	557.535	/	0.006
2	Theoretical	59.118	59.095	82.176	142.913	242.946	253.625	/	0.02
	SIM	59.124	59.100	82.307	143.197	243.429	254.769	1	0.005
	Guyan reduction	59.734	60.463	86.246	496.907	1014.249	950.751	/	0.004
	Kuhar reduction	59.121	59.099	82.220	168.001	497.432	626.606	/	0.006

/: no iterations required.
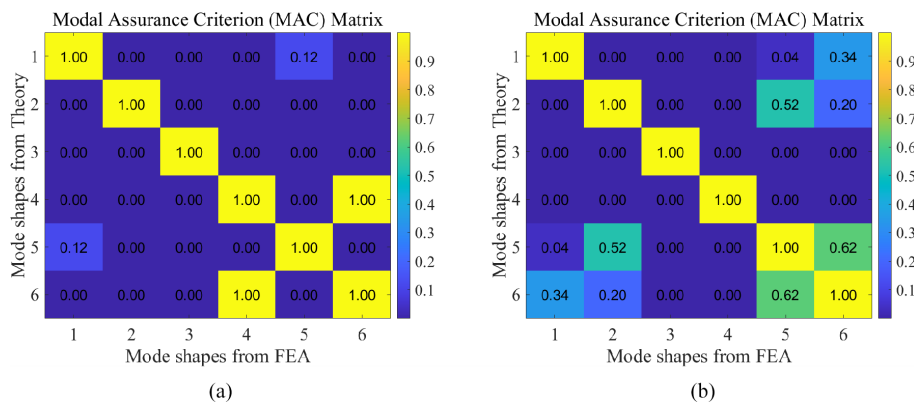
Figure 7. The modal assurance criterion (MAC) values of the modes obtained from the theoretical method and the FEM: **(a)** pose 1 and **(b)** pose 2.
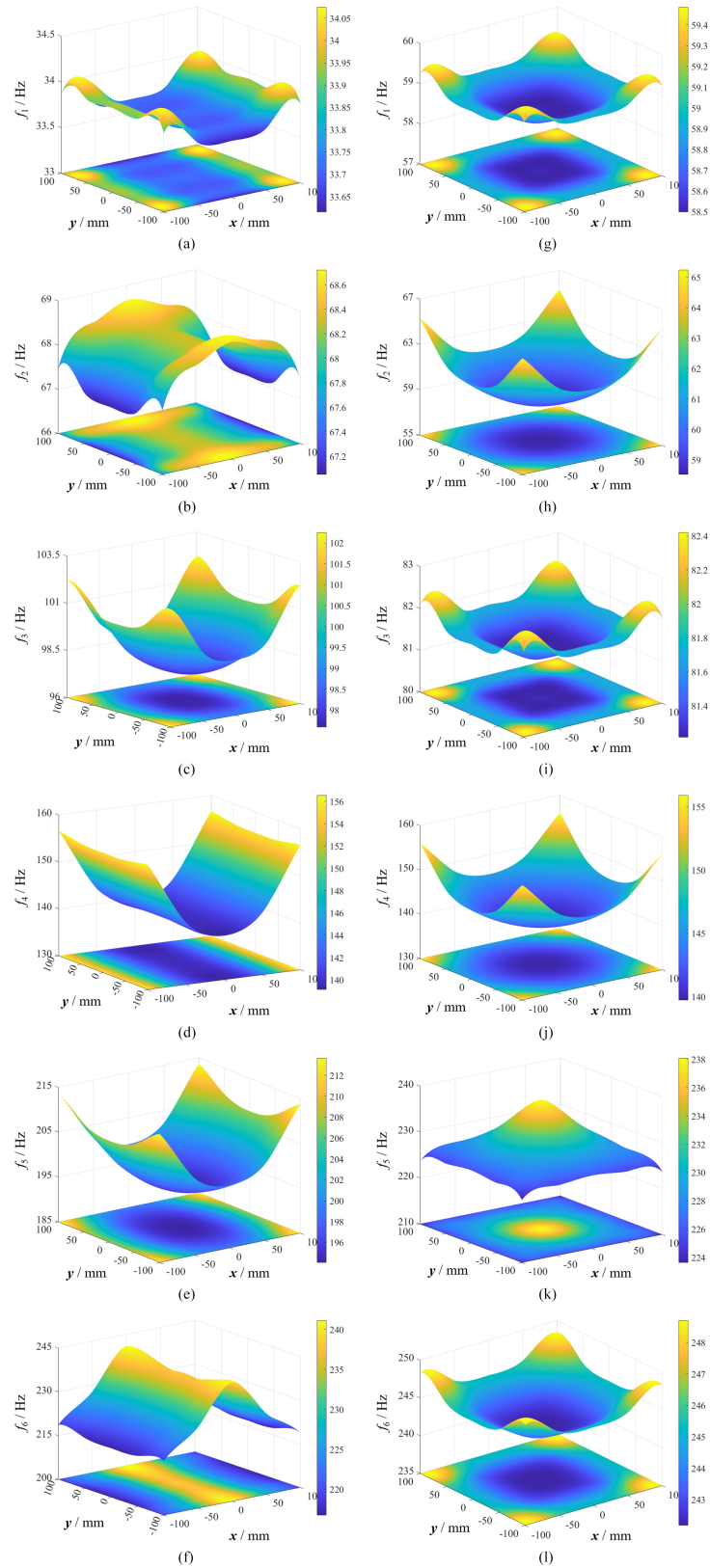
Figure 8. Modal distribution of the 4SRRR parallel robot (pose 1 at $z = 0.35$, pose 2 at $z = 0.40546$): **(a)** pose 1: f_1, **(b)** pose 1: f_2, **(c)** pose 1: f_3, **(d)** pose 1: f_4, **(e)** pose 1: f_5, **(f)** pose 1: f_6, **(g)** pose 2: f_1, **(h)** pose 2: f_2, **(i)** pose 2: f_3, **(j)** pose 2: f_4, **(k)** pose 2: f_5, and **(l)** pose 2: f_6.

over, the first natural frequency in pose 2 has higher values at the four corners of the motion plane.

5 Conclusions

To address the unstructured on-site work requirements in shipyards and large-steel-structure manufacturing plants, this paper develops a 4SRRR quadruped wall-climbing robot. Focusing on the 4SRRR parallel robot, the study first establishes global independent generalized displacement coordinates by combining multipoint constraint elements and linear algebra. Based on these coordinates, the overall mass and stiffness matrices of the robot are constructed, thus obtaining the natural frequencies of the robot. In this research, the moving platform and joints are assumed to be rigid, the spatial elastic deformation of the rods is considered, and Timoshenko beam elements accounting for shear deformation are used to replace Euler–Bernoulli beam elements. The generalized kinetic and potential energies of the elastic deformation of each component are established based on the global independent generalized coordinates. These coordinates encompass the boundary conditions and continuity conditions of the mechanism, having clear physical significance and avoiding the drawbacks of solving a large number of constraint equations simultaneously with the elastodynamic equations.

By comparing the natural frequency calculation results of the theoretical model with those of the finite element model, it is found that even when the rods are considered single elements the error in the first three natural frequencies does not exceed 4 %. When the rods are divided into three elements, the error in the first six natural frequencies does not exceed 4.4 %. Further increasing the number of rod divisions results in no significant reduction in the error. The comparative analysis of the natural frequency calculation results between the theoretical model and the finite element model verifies the correctness of the theoretical model presented in this paper.

In this paper, the joints, actuators, and moving platform are assumed to be rigid, and damping is considered negligible. In future work, the elasticity of the joints, actuators, and moving platform, as well as the damping of the mechanism, will be considered to establish an elastodynamic model that more closely approximates engineering reality, thereby obtaining more accurate results. Additionally, this paper only considers the natural frequency analysis of the 4SRRR quadruped wall-climbing robot. In the future, the combination of the 4SRRR quadruped wall-climbing robot with a 6R welding robotic arm will be considered for natural frequency analysis of the 4SRRR+6R hybrid robot.

Author contributions. XH and YZ conceived and designed the study. BW and YZ conducted investigation. BW and CY performed program coding. BW wrote the article.

References

Cammarata, A., Condorelli, D., and Sinatra, R.: An Algorithm to Study the Elastodynamics of Parallel Kinematic Machines With Lower Kinematic Pairs, J. Mech. Robot., 5, 011004, https://doi.org/10.1115/1.4007705, 2013.

Cheng, L. and Wang, H.: Finite element modal analysis of the FPD glass substrates handling robot, International Conference on Mechatronics and Automation (ICMA), Chengdu, China, 5–8 August 2012, IEEE, 1341–1346, https://doi.org/10.1109/ICMA.2012.6284331, 2012.

Germain, C., Briot, S., Caro, S., and Wenger, P.: Natural Frequency Computation of Parallel Robots, J. Comput. Nonlin. Dyn., 10, 021004, https://doi.org/10.1115/1.4028573, 2015.

Hoevenaars, A. G. L., Krut, S., and Herder, J. L.: Jacobian-based natural frequency analysis of parallel manipulators, Mech. Mach. Theory, 148, 103775, https://doi.org/10.1016/j.mechmachtheory.2019.103775, 2020.

Hou, Y., Zhang, G., and Zeng, D.: An efficient method for the dynamic modeling and analysis of Stewart parallel manipulator based on the screw theory, P. I. Mech. Eng. C-J. Mec., 234, 808–821, https://doi.org/10.1177/0954406219885963, 2020.

Kermanian, A., Kamali, E. A., and Taghvaeipour, A.: Dynamic analysis of flexible parallel robots via enhanced co-rotational and rigid finite element formulations, Mech. Mach. Theory, 139, 144–173, https://doi.org/10.1016/j.mechmachtheory.2019.04.010, 2019.

Korayem, M. H., Dehkordi, S. F., Mojarradi, M., and Monfared, P.: Analytical and experimental investigation of the dynamic behavior of a revolute-prismatic manipulator with N flexible links and hubs, Int. J. Adv. Manuf. Tech., 103, 2235–2256, https://doi.org/10.1007/s00170-019-03421-x, 2019.

Liang, D., Song, Y., Sun, T., and Jin, X.: Rigid-flexible coupling dynamic modeling and investigation of a redundantly actuated parallel manipulator with multiple actuation modes, J. Sound. Vib., 403, 129–151, https://doi.org/10.1016/j.jsv.2017.05.022, 2017.

Lochan, K., Singh, J. P., Roy, B. K., and Subudhi, B.: Adaptive time-varying super-twisting global SMC for projective synchronisation of flexible manipulator, Nonlinear. Dynam., 93, 2071–2088, https://doi.org/10.1007/s11071-018-4308-9, 2018.

Luo, H., Wang, H., Zhang, J., and Li, Q.: Rapid Evaluation for Position-Dependent Dynamics of a 3-DOF PKM Module, Adv. Mech. Eng., 6, 238928, https://doi.org/10.1155/2014/238928, 2014.

Lvov, N., Khabarov, S., Todorov, A., and Barabanov, A.: Versions of fiber-optic sensors for monitoring the technical condition of aircraft structures, Civ. Eng. J., 12, 2895–2902, https://doi.org/10.28991/cej-03091206, 2018.

Ma, Y., Niu, W., Luo, Z., Yin, F., and Huang, T.: Static and dynamic performance evaluation of a 3-DOF spindle head using CAD–CAE integration methodology, Robot. Cim.-Int. Manuf., 41, 1–12, https://doi.org/10.1016/j.rcim.2016.02.006, 2016.

Mei, J. and Zhao, Y.: Elastodynamic-model-based stiffness analysis of a 6-RSS PKM, J. Mech. Sci. Technol., 32, 4447–4459, https://doi.org/10.1007/s12206-018-0842-0, 2018.

Nguyen, V., Cvitanic, T., and Melkote, S.: Data-driven modeling of the modal properties of a 6-DOF industrial robot and its application to robotic milling, J. Manuf. Sci. E.-T. ASME, 141, 121006, https://doi.org/10.1115/1.4045175, 2019.

Pham, M. T., Teo, T. J., and Yeo, S. H.: Synthesis of multiple degrees-of-freedom spatial-motion compliant parallel mechanisms with desired stiffness and dynamics characteristics, Precis. Eng., 47, 131–139, https://doi.org/10.1016/j.precisioneng.2016.07.014, 2017.

Sheng, L., Li, W., Wang, Y., Yang, X., and Fan, M.: Rigid-flexible coupling dynamic model of a flexible planar parallel robot for modal characteristics research, Adv. Mech. Eng., 11, 1–10, https://doi.org/10.1177/1687814018823469, 2019.

Son, H., Choi, H. J., and Park, H. W.: Design and dynamic analysis of an arch-type desktop reconfigurable machine, Int. J. Mach. Tool. Manu., 50, 575–584, https://doi.org/10.1016/j.ijmachtools.2010.02.006, 2010.

Taghvaeipour, A., Angeles, J., and Lessard, L.: Elastodynamics of a two-limb Schonflies motion generator, P. I. Mech. Eng. C-J. Mec., 229, 751–764, https://doi.org/10.1177/0954406214538781, 2015.

Venkiteswaran, K. V. and Su, H. J.: A three-spring pseudorigid-body model for soft joints with significant elongation effects, J. Mech. Robot., 8, 1–7, https://doi.org/10.1115/1.4032862, 2016.

Vu, L. N. and Kuo, C. H.: An analytical stiffness method for spring-articulated planar serial or quasi-serial manipulators under gravity and an arbitrary load, Mech. Mach. Theory, 137, 108–126, https://doi.org/10.1016/j.mechmachtheory.2019.03.015, 2019.

Wu, L., Wang, G., Liu, H., and Huang, T.: An approach for elastodynamic modeling of hybrid robots based on substructure synthesis technique, Mech. Mach. Theory, 123, 124–136, https://doi.org/10.1016/j.mechmachtheory.2017.12.019, 2018.

Yang, C., Li, Q. C., and Chen, Q. H.: Natural frequency analysis of parallel manipulators using global independent generalized displacement coordinates, Mech. Mach. Theory, 156, 104145, https://doi.org/10.1016/j.mechmachtheory.2020.104145, 2021.

Yu, F. and Chen, X.: Dynamic modeling and development of symbolic calculation software for N-DOF flexible-link manipulators incorporating lumped mass, Shock. Vib., 2019, 5627271, https://doi.org/10.1155/2019/5627271, 2019.

Zhang, J. and Zhao, Y. Q.: Elastodynamic modeling and joint reaction prediction for 3-PRS PKM, J. Cent. South Univ., 22, 2971–2979, https://doi.org/10.1007/s11771-015-2833-y, 2015.

Zhang, J., Zhao, Y. Q., and Ceccarelli, M., Elastodynamic Model-Based Vibration Characteristics Prediction of a Three Prismatic–Revolute–Spherical Parallel Kinematic Machine, J. Dyn. Syst.-T. ASME, 138, 041009, https://doi.org/10.1115/1.4032657, 2016.

Zhang, X., Mills, J. K., and Cleghorn, W. L.: Flexible linkage structural vibration control on a 3-PRR planar parallel manipulator: experimental results, P. I. Mech. Eng. I.-J. Sys., 223, 71–84, https://doi.org/10.1243/09596518JSCE594, 2009.

Zhang, Y. and Lin, J.: Fundamentals of structural dynamics, Dalian University of Technology Press, Dalian, China, ISBN 978-7-5611-3570-9, 2007.

Zhao, Y., Gao, F., Dong, X., and Zhao, X.: Dynamics analysis and characteristics of the 8-PSS flexible redundant parallel manipulator, Robot. Cim.-Int. Manuf., 27, 918–928, https://doi.org/10.1016/j.rcim.2011.03.003, 2011.

Zhu, S. and Yu, Y.: Pseudo-rigid-body model for the flexural beam with an inflection point in compliant mechanisms, J. Mech. Robot., 9, 1–8, https://doi.org/10.1115/1.4035986, 2017.